AGU PUBLICATIONS

JGR

Journal of Geophysical Research: Oceans

RESEARCH ARTICLE

10.1002/2016JC012408

On the role of sea-state in bubble-mediated air-sea gas flux during a winter storm

Jun-Hong Liang[1,2,3], Steven R. Emerson[4], Eric A. D'Asaro[5], Craig L. McNeil[5], Ramsey R. Harcourt[5], Peter P. Sullivan[6], Bo Yang[4], and Meghan F. Cronin[7]

[1]Department of Oceanography and Coastal Sciences, Louisiana State University, Baton Rouge, Louisiana, USA, [2]Center for Computation and Technology, Louisiana State University, Baton Rouge, Louisiana, USA, [3]Coastal Studies Institute, Louisiana State University, Baton Rouge, Louisiana, USA, [4]School of Oceanography, University of Washington, Seattle, Washington, USA, [5]Applied Physics Laboratory, University of Washington, Seattle, Washington, USA, [6]National Center for Atmospheric Research, Boulder, Colorado, USA, [7]National Oceanic and Atmospheric Administration Pacific Marine Environmental Laboratory, Seattle, Washington, USA

Key Points:
- Observed gases under a winter storm are reproduced by a bubble-resolving model
- Bubbles play an important role in mixed-layer dissolved gas budgets during the winter storm
- Bubble-mediated gas flux is larger for smaller wave age due to the greater prevalence of large breaking waves in a younger sea

Correspondence to:
J.-H. Liang,
jliang@lsu.edu

Citation:
Liang, J.-H., S. R. Emerson, E. A. D'Asaro, C. L. McNeil, R. R. Harcourt, P. P. Sullivan, B. Yang, and M. F. Cronin (2017), On the role of sea-state in bubble-mediated air-sea gas flux during a winter storm, *J. Geophys. Res. Oceans, 122*, 2671–2685, doi:10.1002/2016JC012408.

Received 30 SEP 2016
Accepted 28 FEB 2017
Accepted article online 2 MAR 2017
Published online 1 APR 2017

Abstract Oceanic bubbles play an important role in the air-sea exchange of weakly soluble gases at moderate to high wind speeds. A Lagrangian bubble model embedded in a large eddy simulation model is developed to study bubbles and their influence on dissolved gases in the upper ocean. The transient evolution of mixed-layer dissolved oxygen and nitrogen gases at Ocean Station Papa (50°N, 145°W) during a winter storm is reproduced with the model. Among different physical processes, gas bubbles are the most important in elevating dissolved gas concentrations during the storm, while atmospheric pressure governs the variability of gas saturation anomaly (the relative departure of dissolved gas concentration from the saturation concentration). For the same wind speed, bubble-mediated gas fluxes are larger during rising wind with smaller wave age than during falling wind with larger wave age. Wave conditions are the primary cause for the bubble gas flux difference: when wind strengthens, waves are less-developed with respect to wind, resulting in more frequent large breaking waves. Bubble generation in large breaking waves is favorable for a large bubble-mediated gas flux. The wave-age dependence is not included in any existing bubble-mediated gas flux parameterizations.

1. Introduction

Air-sea gas exchange is an important process in the earth system. It influences the partitioning of gases between the ocean and the atmosphere. It also determines the mixed-layer gas contents available for advection into the ocean interior and for oceanic biogeochemical cycling. At low wind speeds ($u_{10} < \sim 7$ m s^{-1}), the ocean surface is unbroken and gas exchange is governed by diffusive and turbulent processes within the thin layer close to air-sea interface. Gas exchange in this regime has been relatively well studied by theoretical, laboratory, and field investigations [e.g., *Jähne and Haußecker*, 1998; *Wanninkhof et al.*, 2009]. At moderate to high wind speeds ($u_{10} > \sim 7$ m s^{-1}), gas bubbles entrained into the ocean primarily by breaking waves contribute significantly to the total air-sea gas flux [e.g., *Farmer et al.*, 1993; *Asher et al.*, 1996; *D'Asaro and McNeil*, 2007].

After entrained into the ocean by breaking waves, gas bubbles rise due to their buoyancy, while turbulence acts to trap them inside the surface ocean boundary layer. Bubble plumes penetrating the ocean surface boundary layer are commonly observed with acoustical techniques [e.g., *Farmer and Li*, 1995; *Vagle et al.*, 2010] and are indicative of downward branches of the Langmuir circulations, counter-rotating vortices oriented downwind, that arise from the intraction between surface gravity waves and currents [e.g., *Leibovich*, 1983; *Thorpe*, 2004]. Small bubbles with small buoyant rising speeds are mixed downward and dissolve completely. Large bubbles exchange gases while in the water and eventually burst at the ocean surface. The two end-members, categorized as completely dissolved bubbles and partially dissolved bubbles [e.g., *Fuchs et al.*, 1987; *Keeling*, 1993; *Woolf*, 1997], play different roles in air-sea gas exchange. Intuitively, completely dissolved bubbles can only inject gases into water while partially dissolved bubbles can mediate flux either into or out of the ocean depending on the dissolved gas saturation level. This separation of bubbles is crucial to the development of a mechanistically based gas flux parameterization: gas flux associated

with completely dissolved bubbles is determined only by the air amount in this type of bubble and the atmospheric mole fraction of a gas, while gas flux through partially dissolved bubbles is also influenced by gas solubility, gas diffusivity, bubble properties (e.g., clean or dirty bubbles), and dissolved gas concentration. The bubble effect on air-sea gas flux is larger for less soluble gases and when the wind is stronger. The qualitative role of bubbles is now well understood: bubbles enhance the total air-sea gas transfer rate by providing additional interfaces for gas transfer, i.e., bubble surfaces; and they drive the surface ocean to supersaturation because the total pressure on bubbles includes hydrostatic pressure and surface tension in addition to atmospheric pressure. However, the quantitative role of bubbles is still very uncertain. Several observational and numerical studies [e.g., *Woolf and Thorpe*, 1991; *Hamme and Emerson*, 2002; *McNeil and D'Asaro*, 2007; *Stanley et al*., 2009; *Vagle et al*., 2010; *Nicholson et al*., 2011; *Liang et al*., 2013; *Emerson and Bushinsky*, 2016; *Manning et al*., 2016] have attempted to quantify the effect of gas bubbles on air-sea gas flux. Parameterization from these studies assume that wind speed is the sole factor in determining bubble gas flux, and each parameterization has achieved success in the individual scenarios and data sets studied. However, the evident difference in the quantitative expressions for bubble-mediated gas flux among these studies [see *Liang et al*., 2013, Figure 5] indicates significant underlying uncertainties in those formulas. While the formulation uncertainties can be partially attributed to uncertainties in measurements and models, it may also imply that other factors beyond wind speed play a nonnegligible role in the total gas flux. Considering that bubbles are entrained by breaking waves and the amount and size of breaking waves can differ for the same wind speed, it is plausible that wave conditions are an additional factor influencing bubble-mediated gas flux. *Woolf* [2005] proposed a wave-dependent parameterization for gas transfer rate. According to the parameterization, gas transfer rate is higher when waves are more mature based on the fact that whitecap coverage is larger in a more mature sea.

The objectives of this study are to further our understanding of bubble-mediated gas exchange by (1) improving a mechanistically based modeling framework for the evolution of bubbly flows and gases in the upper ocean; (2) exploring the relative importance of bubbles and other physical processes in determining upper ocean gas concentrations and gas saturation anomalies under storm conditions; and (3) examining qualitatively the influence of wave conditions on bubble-mediated gas flux. To achieve the objectives, the transient evolution of bubbly flows and dissolved gases under a North Pacific winter storm in 2011 is simulated and is compared with in situ observation. Bubble gas fluxes are analyzed. Section 2 describes data; section 3 presents the numerical framework and the way it is configured; section 4 shows the numerical results compared with observations; section 5 discusses the results in section 4; and section 6 is a summary.

2. Data Description

Ocean Station Papa is located at [50°N 145°W], within the subpolar northeastern Pacific gyre close to the Gulf of Alaska, a region of strong and frequent winter storms, and a sink for atmospheric CO_2 [*Fassbender et al*., 2016]. Since summer 2007, the National Oceanic and Atmospheric Administration (NOAA) surface mooring at Station Papa has made continuous high-resolution measurements of environmental conditions on both sides of the air-sea interface [*Cronin et al*., 2015]. Measurements include wind/currents, atmospheric/oceanic temperature, humidity, ocean salinity, atmospheric pressure/seawater gas tension, air and sea partial pressure of CO_2, and radiative fluxes. Critical to this study were the oxygen sensor and gas tension device mounted on the bridle that allow the determination of O_2 and N_2 at a depth of approximately 1 m every 3 h [*Emerson et al*., 2008]. Directional wave spectrum is measured by a nearby waverider buoy since 2010 [*Thomson et al*., 2013]. Physical measurements on the surface mooring were generally sampled at between 1 min and 1 h intervals, with most at 10 min intervals; wave spectrum were sampled every half hour, while biogeochemical and gas measurements were sampled every 3 h.

For the purpose of this study, a 15 day period starting at 12:00 A.M. on 14 November 2011 (GMT) was selected from the available data between summer 2011 and summer 2012. In the first 2 days of this period, the wind speed was low and U_{10} was mostly below 5 m s^{-1} (Figure 1a). Between day 2.5 and day 3, the wind strengthened and U_{10} increased to more than 20 m s^{-1}. At the same time, there was a strong net cooling flux ($\sim$450 W m^{-2}) due primarily to strong sensible and latent heat fluxes at the ocean surface associated with the strong winds (Figure 1b). After day 3, the winds gradually weakened while fluctuating. During most of the 15 day period, surface gravity waves were well developed with wave age (c_p/u_* with c_p the

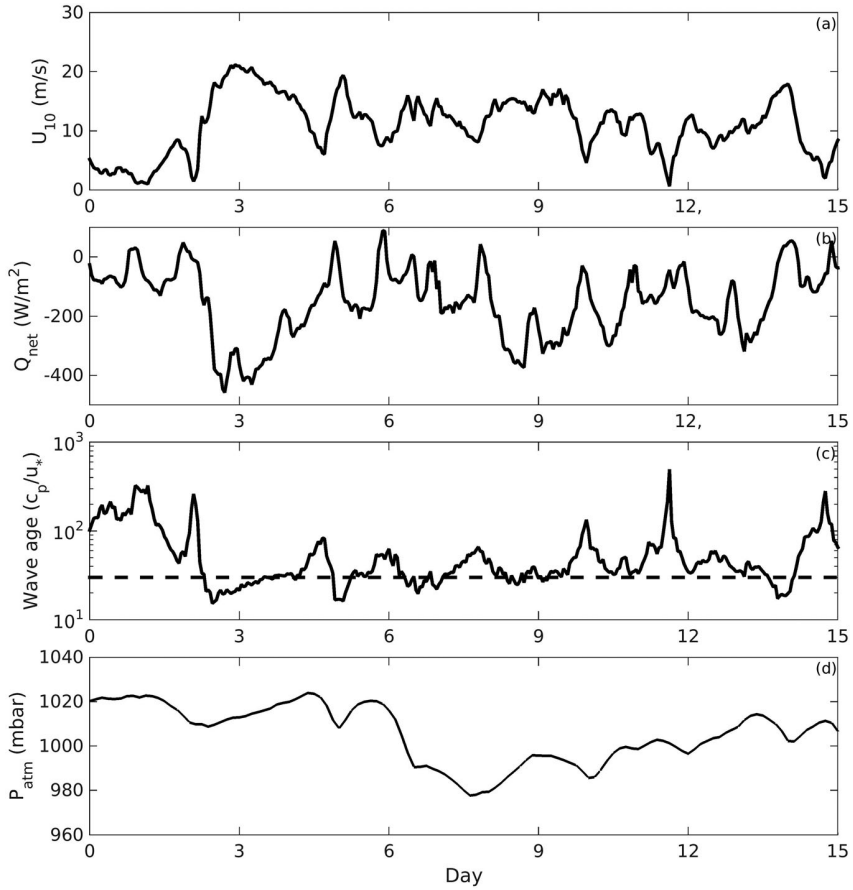

Figure 1. Meteorological conditions: (a) 10 m wind speed, (b) net heat flux, (c) wave age, and (d) sea level pressure for a 15 day period in November 2011. Day 0 corresponds to 12:00 A.M., 14 November 2011. The dashed line in Figure 1b indicates the critical wave age ($c_p/u_* = 30$) *when waves are fully developed. When wave age is larger than 30, waves are mature. When wave age is smaller than 30, waves are not fully developed.*

peak wave phase speed and u_* the atmospheric friction velocity) larger than 30. During periods when the wind increased drastically, i.e., between day 2.5 and day 3, day 5 and day 5.5, and day 13 and day 14, waves were less-developed with respect to the wind and wave age was smaller than 30 (Figure 1c). Atmospheric pressure was close to standard atmospheric pressure (1013.25 mb) in the first 6 days, although there was a slight decrease (∼10 mb or 1%) at the beginning of day 3 before the wind strengthened. After day 6, atmospheric pressure dropped sharply by about 3% to approximately 980 mb on day 8 (Figure 1d) and gradually recovered until day 15. The concurrent high-frequency measurements of meteorological conditions, waves, subsurface hydrography, and gases permit a detailed examination of air-sea gas transfer processes and comparisons with process-oriented computer models. The relatively high wind speed and the variable wave conditions guarantee a noticeable bubble effect and enable our investigation of the influence of wave.

3. Model Description

The numerical model uses large eddy simulation (LES) techniques, coupled with explicit calculations for gas bubbles and dissolved gases. In particular, the model has a dynamic component, a dissolved gas component, and a bubble component. The model framework is described in *Liang et al*. [2011] except that the bubble component has been improved by simulating bubbles as a representative Lagrangian ensemble, rather than as a set of Eulerian fields in discrete bulk size classes.

The ocean model is the National Center for Atmospheric Research large eddy simulation (NCAR-LES) model [e.g., *Moeng*, 1984; *McWilliams et al*., 1997]. It solves the modified incompressible Navier-Stokes equations,

including the phase-averaged effects of surface gravity waves by means of the Craik-Leibovich vortex force [e.g., *Craik and Leibovich*, 1976; *Suzuki and Fox-Kemper*, 2016]. Bubbles-induced buoyancy change is included in the model as a density anomaly in the dynamical equations [*Liang et al*., 2012]. The LES model simulates the turbulent large eddies in the oceanic surface boundary layer explicitly, particularly Langmuir circulations that deepen the mixed layer and trap buoyant bubbles in downwelling convergence zones. The NCAR-LES model has been used to explore oceanic boundary layer turbulence under a range of surface and lateral influences [e.g., *Sullivan and McWilliams*, 2010; *Van Roekel et al*., 2012; *Kukulka et al*., 2013; *Hamlington et al*., 2014]. Detailed model formulations have been reported in existing publications [e.g., *McWilliams et al*., 1997; *Sullivan et al*., 2007] and are not repeated here. The LES model provides the turbulence and temperature environment for the evolution of dissolved gases and bubbles.

Dissolved gas concentrations are modeled as passive tracers by solving advection-diffusion equations. Gases are advected by turbulent flow fields resolved in the LES model, and diffused in conjunction with the LES subgrid model for unresolved turbulence. Sources and sinks for dissolved gases include air-sea diffusive gas fluxes at the ocean surface, bubble gas fluxes provided by the bubble model. Biogeochemical effects on both O_2 [*Bushinsky and Emerson*, 2015] and N_2 [*Emerson et al*., 2002] in the winter-time subarctic North Pacific surface water are small compared to the contribution from air-sea gas flux in the relatively short period examined here and are neglected in the model. Here gas bubbles are modeled in a Lagrangian framework and are tracked as a number (approximately 8 million for the simulations shown below) of individual "superbubbles," each of which represents a certain amount of actual bubbles. For each Lagrangian superbubble, a set of ordinary differential equations (ODEs) for its location ($\mathbf{x}$), gas amounts (n_j with $j = 1$ and 2 for O_2 and N_2, respectively) and radius (r) are integrated [e.g., *Woolf and Thorpe*, 1991; *Baschek et al*., 2006]:

$$\frac{d\mathbf{x}}{dt} = \mathbf{u} = \mathbf{u}_r + \mathbf{u}_s + w_b \tag{1}$$

$$\frac{dn_j}{dt} = -4\pi r^2 k_{bub}\left[S_j \chi_j \left(p_w + p_{atm} + \frac{2\gamma}{r}\right) - c_{wj}\right] \tag{2}$$

$$\frac{dr}{dt} = \left[\frac{3RT}{4\pi r^2}\sum_j \frac{dn_j}{dt} - r\frac{dp_{tot}}{dt}\right]\left(3p + 3p_{atm} + \frac{4\gamma}{r}\right)^{-1} \tag{3}$$

In equation (1) for the Lagrangian trajectory, the resolved velocity ($\mathbf{u}_r$) is interpolated from the LES solutions; bubble buoyant rising speed (w_b) follows the size-dependent formula suggested by *Woolf and Thorpe* [1991]; the subgrid-scale velocity ($\mathbf{u}_s$) is calculated by integrating a stochastic differential equation following *Weil et al*. [2004]:

$$du_{s,i} = -\frac{f_s C_0 \varepsilon}{2}\frac{u_{s,i}}{\sigma_s^2}dt + \frac{1}{2}\left(\frac{1}{\sigma_s^2}\frac{d\sigma_s^2}{dt}u_{s,i} + \frac{\partial \sigma_s^2}{\partial x_i}\right)dt + (f_s C_0 \varepsilon)^{1/2} d\xi_i \tag{4}$$

where $\sigma_s^2 = 2e_s/3$ is the isotropic stress with e_s the subgrid-scale turbulent kinetic energy from the LES model; ε is dissipation rate, and $d\xi_i$ is a Gaussian white noise. Following the parameterization of *Weil et al*. [2004] as, $f_s = \langle \sigma_s^2 \rangle / \left(\langle \sigma_{av}^2 \rangle + \langle \sigma_s^2 \rangle\right)$ with σ_{av}^2 the resolved velocity variance, and subscript i indicates horizontal dimension. The subgrid-scale velocity is negligible except close to the surface where turbulence is poorly resolved. In equation (2) for gas amount in bubbles, gas transfer rate through individual bubbles (k_{bub}) is calculated with the formulas proposed by *Leifer and Patro* [2002]; S_j is gas solubility; $\chi_j = \frac{n_j}{\sum n_j}$ is the atmospheric fraction of gas j; p_w is the water pressure; p_{atm} is atmospheric pressure, γ is the surface tension coefficient; and c_{wj} is the concentration of dissolved gases around the superbubble interpolated from the dissolved gas model. The turbulence fields, temperature field, and gas fields at each time step from the dynamic and the dissolved gas model are used to drive the bubble model, while the gas fluxes from the bubble model are sources and sinks to the dissolved gas model. The bubble model is embedded in the parallelized framework of the NCAR-LES model. Each superbubble is assigned to the processor that solves the dynamic and the dissolved gas equations for the grid block where the superbubble is at. When the superbubble moves from one grid block to a neighboring grid block, its information is passed to the processor responsible for the neighboring grid block. Compared with an Eulerian bubble concentration model [e.g., *Liang et al*., 2011, 2012; *Ma et al*., 2011], a Lagrangian model has the following advantages: (1) physically, a Lagrangian model

allows straightforward diagnosis of gas fluxes through completely dissolved bubbles and through partially dissolved bubbles since the fate of individual bubbles is tracked; (2) numerically, a Lagrangian model more accurately solves a suite of ordinary differential equations, avoiding nonphysical solutions associated with the dispersive and diffusive errors inherent to numerical solutions of advection-diffusion equations in an Eulerian model; and (3) computationally, it is more efficient as computing power is allocated only to locations where bubbles are abundant, while bubble concentrations are calculated at each grid point in an Eulerian coordinate system, even at depths where bubbles seldom penetrate to.

Bubbles are entrained into the ocean during breaking waves. While the detailed wave breaking and air entrainment are not resolved in the simulation, their integral effects on bubble deposition, as input forcing conditions for the simulations, are obtained by using the stochastic breaking wave model of *Sullivan et al*. [2007], forced by available observations. In the breaking wave model, the breaking wave energy flux ($\mathcal{E}$) is calculated as $\mathcal{E}=\tau u_* \bar{c}$ where τ is the wind stress and $\bar{c}$ is a parameter dependent on wave age [*Terray et al*., 1996]. According to observations [*Terray et al*., 1996; see Figure 8 therein], $\bar{c}=3.9$ for mature seas ($c_p/u_* > 30$). During rising winds, $\bar{c}$ increases with decreasing wave age (c_p/u_*). It reaches its maximum, around 8, when c_p/u reaches 15, approximately the minimum wave age in the selected 15 day period (Figure 1c). When wave age further decreases ($c_p/u_* < 15$), $\bar{c}$ also decreases. Under each individual breaking wave, bubble deposition follows the spatial and temporal distributions proposed by *Sullivan et al*. [2004, equations 3.1 to 3.3], which is designed to match observed flow structures under breaking waves [*Melville et al*., 2002]. Vertically, bubble deposition spans 0.1 of the breaking-wave length, consistent with laboratory and numerical studies [e.g., *Lamarre and Melville*, 1991; L. Deike, personal communication, 2016]. The size of breaking waves follows a wave-age-dependent distribution function $P(c_b)=b_1 \exp(-b_2 c_b/u_*)$ with c_b the breaker speed. The exponential breaking wave distribution function was proposed by *Melville and Matusov* [2002] based on aerial observations of breaking waves. While breakers with a range of c_b contribute to both momentum and energy fluxes, only those with c_b larger than 3 m s^{-1} are visible and contribute to air entrainment [*Sutherland and Melville*, 2013]. Coefficient b_1 ensures that $\int P(c_b)dc_b=1$. Coefficient b_2 is constrained by the relationship between wave momentum flux and wave energy flux by *Terray et al*. [1996] and is wave-age dependent [see *Sullivan et al*., 2007 for details]. It is smaller for larger $\bar{c}$, indicating relatively less smaller and much larger breaking waves when wave age is low, a result in agreement with more recent observations [*Sutherland and Melville*, 2013, 2015]. Consequently, bubbles are entrained to greater depths in young (wind) seas than in fully developed seas. Computed near-surface dissipation rate with the breaking wave distribution function is in good agreement with observations [see *Sullivan et al*., 2007, Figure 11]. The amount of air in deposited bubbles is calculated by assuming that the gravitational work needed to push gas bubbles into water is a certain fraction (α_b) of the breaking wave energy flux ($\mathcal{E}$). Laboratory and numerical experiments [e.g., *Lamarre and Melville*, 1991; *Blenkinsopp and Chaplin*, 2007; *Deike et al*., 2016] show that α_b spans a range of values, primarily depending on the type of breaking waves. Recent studies [e.g., *Deike et al*., 2016] suggest that α_b lies between 5% and 15%. In this study, the fraction (α_b) is chosen to best match observed gas concentrations and is found to be 8% in the course of several trial simulations. Deposited bubble size distribution ($R(r)$) follows measurements by *Deane and Stokes* [2002], i.e., $R(r) \propto r^{-3/2}$ for $r \geq r_H$, and $R(r) \propto r^{-10/3}$ for $r < r_H$ where r_H is the Hinze scale [*Hinze*, 1955]. When bubbles are smaller than the Hinze scale, surface tension is sufficiently large to resist turbulent shear and fragmentation. The Hinze scale depends on dissipation rate (ε) as $r_H=0.5(\gamma/\rho)^{3/5}\varepsilon^{-2/5}$ [e.g., *Deane and Stokes*, 2002; *Deike et al*., 2016]. Horizontally, the location of bubble deposition is uniformly random. Through a series of parameter sensitivity simulations, we found that the value of α_b controls the magnitude of bubble effect. If any other parameter in the bubble model is changed, α_b has to be adjusted accordingly. For example, if the deposition depth increases or decreases by 50% (0.15 wave length or 0.05 wave length), α_b needs to decrease by 15% or increase by 5% to best match observed gas concentrations and is within [5% 15%] suggested by *Deike et al*. [2016].

Numerical solutions for the selected period are obtained by driving the model with the observed meteorological forcing (Figure 1). The model is configured on a rectangular domain of 300 m × 300 m × 200 m with 160 × 160 × 128 grids. Initial stratification (12:00 A.M. 14 November 2011) is obtained from observations at the mooring (Figure 2a), with an initial mixed layer around 60 m deep. Initial O_2 and N_2 concentrations in the mixed layer are set to mooring observations since production and consumption of the two gases due to air-sea exchange and biogeochemical processes are much slower than turbulent processes

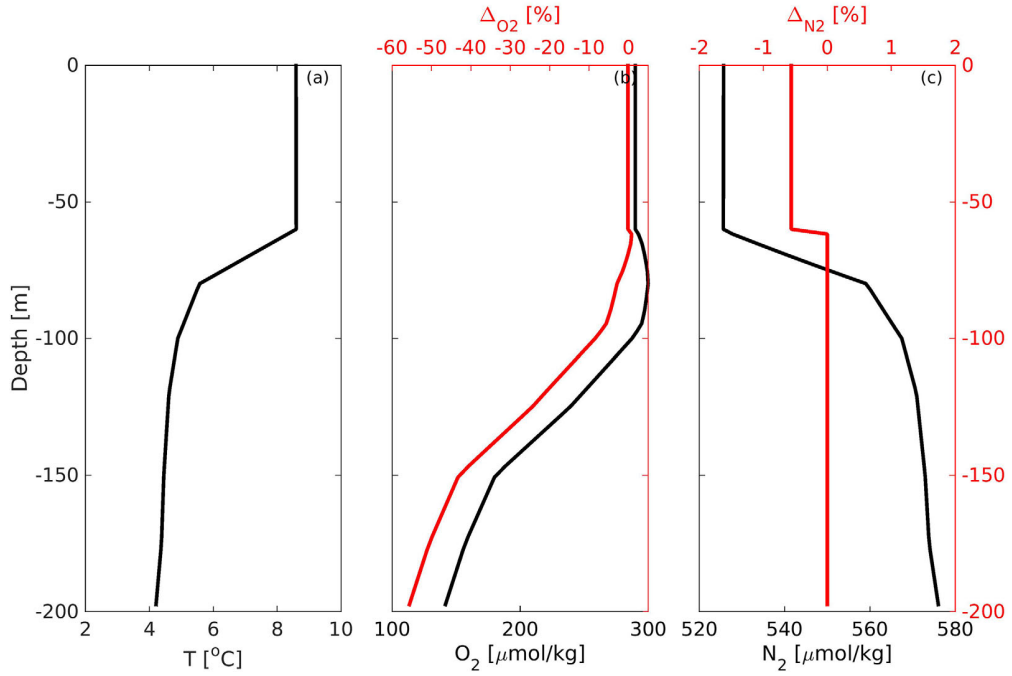

Figure 2. Initial profiles of (a) temperature, (b) O_2 concentration and saturation anomaly, and (c) N_2 concentration and saturation anomaly for the simulations.

within the layer and gas concentration is uniform within the layer. Below the mixed layer, O_2 is linearly interpolated from the November climatology from the World Ocean Atlas 2013 [*Garcia et al.*, 2014] (Figure 2b). In this study, saturation anomaly is defined as

$$\Delta = \left(\frac{C}{C_{sat}{}^{P}/_{P_0}} - 1 \right) \times 100\% \tag{5}$$

where C_{sat} is saturation concentration, P is atmospheric pressure, and $P_0 = 1013.25$ mbar is the standard atmospheric pressure. The definition of Δ is slightly different from that in other literatures [e.g., *Nicholson et al.*, 2010] in that Δ changes with atmospheric pressure. Right below the mixed layer, between 60 and approximately 90 m, O_2 concentration is slightly higher than within the mixed layer, although it is still undersaturated. Within this layer, O_2 is produced during summer when light penetrates to this depth and photosynthetic O_2 production partially compensates for respiratory consumption. Below 90 m, O_2 decreases with depth due to respiration. Initial N_2 concentration is assumed to be 100% saturated with respect to standard atmospheric pressure, and its concentration increases with depth as temperature decreases (Figure 2c). Initial turbulent velocity and pressure fields are obtained by spinning up the model with steady meteorological conditions at the beginning of the selected period. Surface momentum and buoyancy fluxes are calculated with the COARE-3.0 algorithm [e.g., *Fairall et al.*, 2003]. A few other algorithms (not shown) have also been tested and fluxes using the COARE-3.0 algorithm produce generally superior model skill against observed hydrographic evolution. The time-dependent wave-induced Stokes drift is calculated as [e.g., *Sullivan et al.*, 2007; *Harcourt and D'Asaro*, 2008; *Rabe et al.*, 2015] $\boldsymbol{u}_{st}(z) = 2\int_0^{\pi}\int_{-\pi}^{\pi} \boldsymbol{k}\omega F(\omega,\theta) e^{2|\boldsymbol{k}|z} d\theta d\omega$, where $F(\omega, \theta)$ is the wave directional spectrum from concurrent measurements by a nearby waverider [*Thomson et al.*, 2013]; ω is the wave frequency; θ is the wave propagation direction; and $\mathbf{k}$ is the horizontal wave number vector. Two simulations, differing in the treatment of gas fluxes, are carried out. The first simulation does not simulate bubbles, but instead uses the gas flux parameterization by *Wanninkhof* [1992], which is widely used in both climate models [e.g., *Long et al.*, 2013] and the interpretation of observations [e.g., *Takahashi et al.*, 2002]. In the algorithm, the total ocean-atmosphere gas flux (F_T) is calculated as $F_T = k_T \left({}^{P}/_{P_0} C_{sat} - C \right)$, where $k_T = 0.31 U_{10}^2 \left(\frac{Sc}{660}\right)^{-0.5}$ for Schmidt number Sc; atmospheric pressure P, standard

atmospheric pressure P_0, gas saturation concentration C_{sat} that is inversely related to temperature for both O_2 and N_2, and dissolved gas concentration C. The total gas transfer rate (k_T) here implicitly includes both surface gas transfer rate (k_s) and bubble-enhanced gas transfer rate (k_b). The algorithm represents a common practice in climate models where bubble-enhanced gas transfer rate (k_b) is implicitly retained while bubble-induced supersaturation conditions are neglected (some algorithms, such as the COARE gas algorithm [e.g., *Fairall et al*., 2011] explicitly separate k_b and k_s) [e.g., *Wanninkhof et al*., 2009; *Ho et al*., 2011]. In the second simulation, gas bubbles are explicitly simulated. The bubble gas flux (F_b) is diagnosed from the simulated bubble fields at each time step, while the surface gas flux (F_b) is calculated as $F_s = k_s\left({}^{P}/_{P_0}C_{sat} - C\right)$ with the surface gas transfer rate (k_s) calculated after *Goddijn-Murphy et al*. [2012, 2016] as $k_{s,660} = 2.6U_{10} - 5.7$. The formula is derived from the air-sea gas transfer rate of dimethyl sulfide (DMS) when $U_{10} < 15$ m s^{-1}, assuming the contribution from gas bubbles is negligible for DMS because of its high solubility. Since the physical process for surface gas transfer is the same for wind speed above or below 15 m s^{-1}, the formula by *Goddijn-Murphy et al*. [2012] is applied to all wind speeds in this study.

4. Results

Mixed-layer temperature changes little over the first 2 days. During this period, both wind and cooling are weak, with wind speed mostly below 5 m s^{-1}and surface heat flux cooling by less than 100 W m^{-2}. The mixed layer then cools by about 0.6°C between day 2.5 and day 4 (Figure 3) when wind speeds are more than 20 m s^{-1} and cooling flux more than 400 W m^{-2}. Both entrainment of subsurface cooler water and surface cooling contribute to the mixed-layer temperature change. After day 5, the wind levels off and weakens gradually but is still above 10 m s^{-1} except for a few brief periods. The ocean surface continues to cool by about 0.7°C over the next 10 days, but not as dramatically as during the strongest wind. The solutions (black line in Figure 3) agree well with the observations (red line in Figure 3), particularly during the first 9 days, implying that boundary layer processes dominate the evolution of mixed-layer environment during this period. There are a cooling between day 9 and day 10, and a subsequent warming between day 11 and day 12 not captured by the model. This is likely caused by larger-scale processes, such as eddies and fronts, not included in the model. The reasonable agreement indicates that the dynamic model component provides a credible oceanic environment for the bubble and gas components to evolve.

Vertical velocity variance is a measure of vertical mixing and represents the ability of the turbulence to trap buoyant bubbles. In general, it is larger during higher winds and follows the pattern of wind speeds (Figure 4a). A closer examination by plotting vertical velocity variance against wind speed (Figure 4b) shows that vertical velocity variance is smaller when the wind is strengthening (from day 2 to day 3) than when the wind is weakening (from day 3 to day 4.5). When wind strengthens, waves are limited by fetch and duration and are not fully developed with respect to concurrent wind. Langmuir turbulence driven by waves is weaker in a young sea than in a mature sea [e.g., *Li et al*., 2005; *Harcourt and D'Asaro*, 2008], implying that turbulent flow is less able to subduct bubbles during rising wind. A sensitivity test (not shown) without the effect of surface gravity waves, i.e., no Stokes drift, underestimates the cooling, further confirming the importance of wave-driven Langmuir turbulence in upper ocean mixing during the storm event.

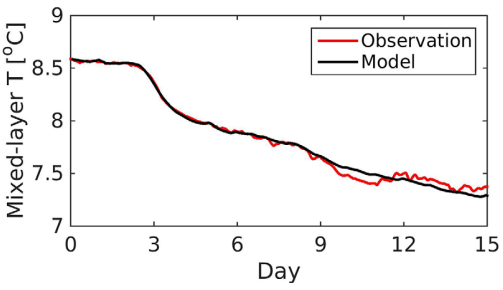

Figure 3. Evolution of observed (red line) and simulated (black line) mixed-layer temperature.

Bubbles are entrained into the ocean by breaking waves and are subsequently advected by boundary layer turbulence. During the period with the strongest winds ($U_{10} > 20$ m s^{-1}), bubble plumes penetrate to more than 25 m (Figure 5a). Since bubbles are buoyant, bubble plumes imply strong and coherent downward currents which are likely the downward branches of Langmuir circulations. In some studies [e.g., *Farmer and Li*, 1995], the bubble plumes have been used to study the structure of Langmuir circulations. Since bubbles are injected randomly in horizontal dimensions, there is no correlation between bubble injection and downward branches

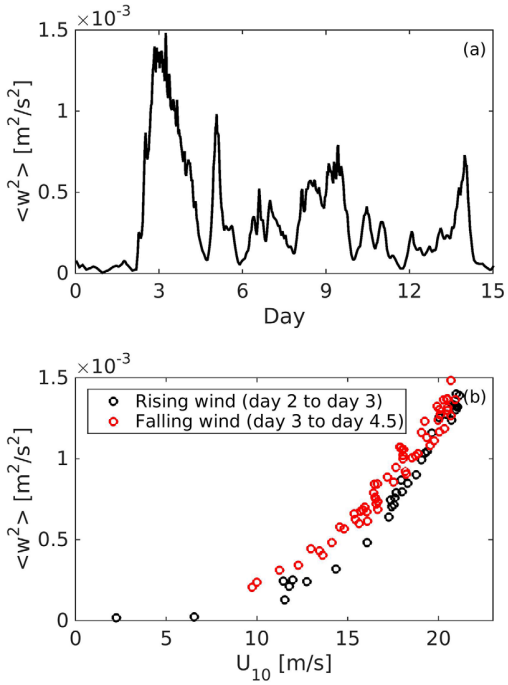

Figure 4. (a) Evolution of simulated mixed-layer averaged vertical velocity variances $<w^2>$; (b) vertical velocity variance versus wind speed during rising wind (black circles) and during falling wind (red circles).

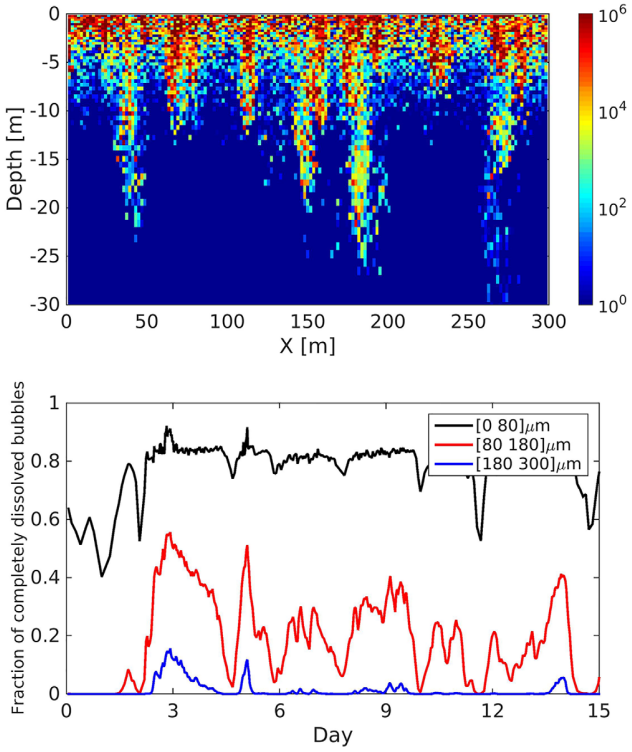

Figure 5. (a) Instantaneous snapshot of bubble number density (number per m^3) at day 3.04 of the simulation when $U_{10} = 21.0$ m s^{-1}. (b) Fraction of completely dissolved bubbles for initial (injection) radius of [0 80] μm (black line), [80 180] μm (red line), and [180 300] μm (blue line).

of Langmuir circulations. During the 15 day period in this study, bubble penetration changes with meteorological conditions. In general, bubbles penetrate deeper when wind speed is higher. The partitioning between complete and partial dissolution for bubbles of different sizes also changes with the meteorological forcing (Figure 5b). Overall, more bubbles end up completely dissolved when the wind is stronger. The change in the bubble partitioning is most evident for bubbles that are initially 80–180 μm in radius for the meteorological conditions during the 15 day period. These bubbles have buoyant rising speeds of centimeters per second that are of the same order of magnitude as turbulent vertical velocities (Figure 4). Smaller bubbles have a smaller buoyant rising speeds and larger surface tension. Many of them completely dissolve at $U_{10} < 10$ m s^{-1}. Larger bubbles require stronger turbulence and coherent structures to trap them.

As with temperature, both dissolved N_2 and O_2 concentrations (C) show little change during the first 2 days and elevate significantly between day 2.5 and day 4 (Figures 6a and 6b). Between day 6 and day 9, the concentration of O_2 decreases although the wind is above 10 m s^{-1}, while there is little decrease in N_2. After day 12, the concentrations of both gases gradually increase again. Gas saturation anomaly shows distinctly different variability from gas concentration. Saturation anomalies for both gases do not noticeably increase between day 2.5 and day 4 (Figures 6c and 6d) as the gas concentrations are going through the most dramatic change. From day 6 to day 8, gas saturation anomalies increase from near saturation to more than 3% supersaturation for both gases, even as gas concentration decreases slightly during the same period. This increase in saturation anomalies coincides with the drop in atmospheric pressure (Figure 1d). After day 8, saturation anomaly gradually decreases, approaching saturation after day 12. The model that

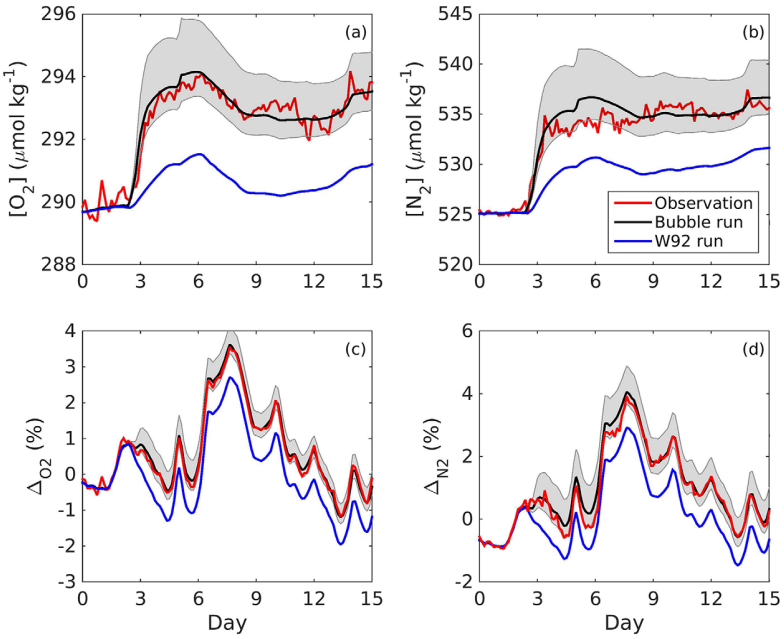

Figure 6. The evolution of (a, b) mixed-layer concentrations and (c, d) supersaturation. Different lines represent: observations (red lines), simulation without bubbles (blue lines), and simulation with bubbles (black lines) for (a, c) O_2 and (b, d) N_2.

explicitly includes bubbles reproduces the observations of both dissolved gas concentration and saturation anomaly reasonably well when $\alpha_b = 8\%$. A larger or smaller α_b leads to an overestimate or underestimate of gas concentrations and saturation anomalies, respectively, indicating the importance of the parameter in the simulated results. The model without bubbles underestimates both quantities after day 3 when the wind strengthens even though it implicitly includes a bubble-enhanced gas transfer rate. While the parameterization by *Wanninkhof* [1992] is used for comparison in this study, other parameterizations without explicit consideration of bubble-induced equilibrium supersaturation will also underestimate both gas concentration and saturation.

Dissolved gas concentration in the upper ocean is modified by air-sea surface diffusive gas fluxes, bubble gas fluxes, mixed-layer entrainment, and biogeochemical processes. The budget for mixed-layer gas concentration (C) can be written as

$$h_{ml}\frac{dC}{dt} = F_e + F_S + F_P + F_C + J \tag{6}$$

where h_{ml} is mixed-layer depth; the left-hand side is the rate of change of gas concentrations; the terms on the right-hand side represent the contributions from mixed-layer entrainment (F_e), surface gas flux (F_s), gas flux through partially dissolved bubbles (F_P), gas flux through completely dissolved bubbles (F_C), and biogeochemical effects (J). Even though the water is slightly supersaturated from day 2.5 to day 4, bubbles are able to add both gases and play the most important role in the mixed-layer gas concentration hikes (Figures 7a and 7b). Entrainment also contributes to the increases in mixed-layer gas concentration, but this effect is secondary to the bubble gas flux. Between day 2.5 and day 3.5 when bubble gas fluxes are the largest, the gas flux through partially dissolved bubbles is larger than the gas flux through completely dissolved bubbles. The significance of partially dissolved bubble leads to a relatively small change in the N_2 to O_2 ratio. If completely dissolved bubbles were to play a more important role, the N_2 to O_2 bubble gas flux ratio would be larger because the solubility of N_2 is about one half that of O_2. There is a similar, but shorter-term gas injection at day 5. Strong surface outgassing is the main cause for gas concentration decrease between day 6 and day 9, indicating that the supersaturation conditions (3% for O_2 and almost 4% for N_2) exceed the equilibrium saturation anomaly during the period. There is a short period around day 8 (not evident in the figure due to its small magnitude) where partially dissolved bubbles also contribute to outgassing. Although bubbles still add gases into the ocean during most of this period, change in gas concentrations is

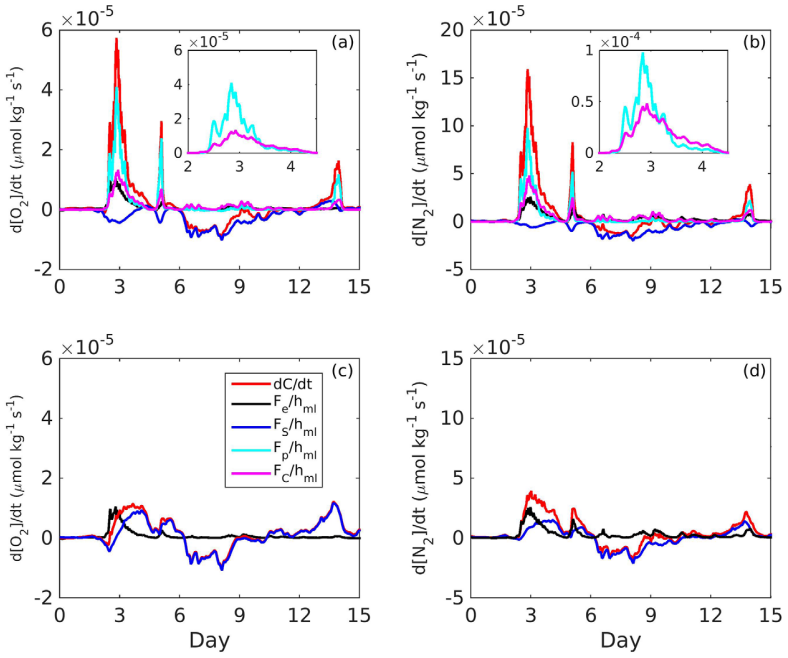

Figure 7. Evolution of mixed-layer dissolved gas budgets for (a, c) O_2 and (b, d) N_2. Figures 7a and 7b are for the run with bubbles while Figures 7c and 7d are for the run without bubbles. The budget equation is defined in equation (6). dC/dt is the rate of change of gas concentrations; F_e/h_{ml} is the effect of bottom entrainment; F_s/h_{ml} is the effect of surface gas flux; F_P/h_{ml} is the effect of flux through partially dissolved bubbles; and F_C/h_{ml} is the effect of flux through completely dissolved bubbles. The insets are zoom-in views of F_P/h_{ml} and F_C/h_{ml} between day 2 and day 4.5.

dominated by the surface outgassing flux. When there are no bubbles, gas injection is smaller between day 2.5 and day 3 and is mainly through entrainment and surface gas flux (Figures 7c and 7d). After day 6, the total air-sea gas flux, including surface and bubble effects, is similar between the runs with and without gas bubbles. The difference in gas contents and saturation anomalies between the two runs changes little after day 6 (Figure 6), although both quantities are different between two runs. During this period, saturation is relatively low and the period of supersaturation is relatively short in the run without bubbles. Surface gas flux contributes to outgassing most of the time in the runs with bubbles, while it is an important source of mixed-layer gas contents in substantial periods in the run without bubbles. In global climate simulations, a run using parameterization without bubble-induced supersaturation will underestimate oceanic gas contents and gas saturation anomalies. However, such a simulation may predict a similar net gas flux to one using parameterization including bubble-induced supersaturation effect.

Both surface gas flux (F_S) and gas flux through partially dissolved bubbles (F_P) are proportional to saturation anomaly (Δ). The evolution of Δ can be understood by taking the temporal derivative of equation (5),

$$\frac{d\Delta}{dt}=\left(\frac{dC}{dt}\frac{1}{{C_{sat}}^{P}/_{P_0}}-\frac{dC_{sat}}{dt}\frac{C}{{C_{sat}}^{2\,P}/_{P_0}}-\frac{dP}{dt}\frac{C}{{C_{sat}}^{P2}/_{P_0}}\right)\times 100\% \tag{7}$$

The first term on the right is the effect of gas concentration change, and it is influenced by the five processes modifying C described by terms on the left-hand side of equation (6). The second term on the right is the contribution from changes in the saturation concentration level, which is largely controlled by temperature and so modified by surface heating/cooling and/or entrainment of subsurface water. The third term is the effect of atmospheric pressure change. The contribution of each term is measured by the relative difference between the individual contribution to the total change in Δ, i.e., $D_k=\int\sqrt{\left(r_k-\frac{d\Delta}{dt}\right)^2}dt/\int\sqrt{\left(\frac{d\Delta}{dt}\right)^2}dt$ where r_k stands for the kth right-hand side term in equation (6). The respective values of D_1–D_3 are 1.11, 0.99, and 0.17 for N_2 and 1.06, 0.95, and 0.14 for O_2. The pressure effect dominates the evolution of Δ, as shown in Figure 8 for the case with bubbles. High-frequency variability in Δ is mostly associated with synoptic variability in atmospheric pressure. The effect of saturation anomaly change is mostly negative during the period as both entrainment and surface cooling during the winter storm elevate saturation

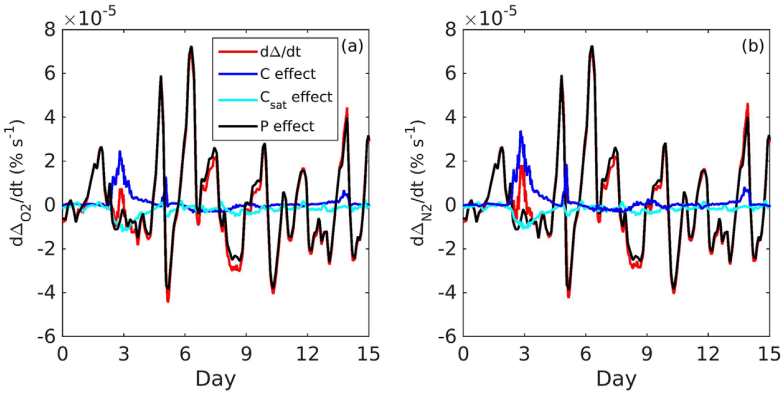

Figure 8. Evolution of mixed-layer saturation anomaly budgets for (a) O_2 and (b) N_2 for the simulation with bubbles. The component terms are as defined for the budget equation (7).

concentration level. The saturation concentration effect due to entrainment is largely balanced by the gas content effect for N_2 as the cooler subsurface water is saturated and is also more enriched in gases (Figure 2b). For O_2, gas concentration increases due to entrainment also works against saturation concentration increase due to the same process. This compensation is fractional since O_2 is undersaturated below the mixed layer, though still larger than within the mixed layer (Figure 2c). The gas content effect is most evident from day 3 to day 4 when bubbles added a large flux of gases into the ocean. All existing parameterizations for bubble-mediated gas fluxes in forecasting models assume that the bubble fluxes (F_p and F_c) depend solely on wind speed [see *Liang et al.*, 2013, Table 1] for the same gas saturations. This assumption is tested by plotting the total bubble-mediated gas flux ($F_p + F_c$) against wind speed (U_{10}) between day 2 and day 4.5 (Figure 9). For the same wind speed, bubble gas fluxes between day 2 and day 3 when the wind strengthens are distinctly larger than fluxes after day 3 when the wind levels off and weakens. As the

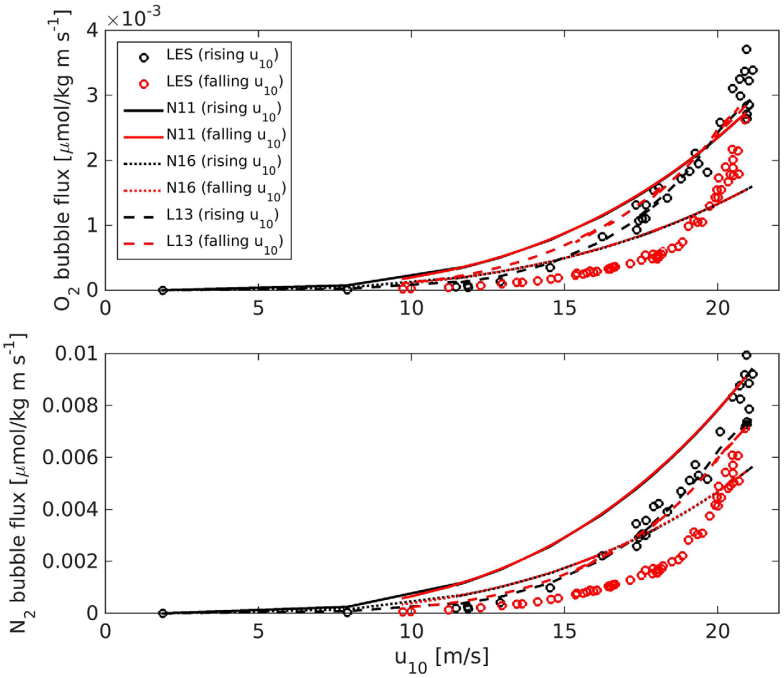

Figure 9. Relationship between bubble gas flux and wind speed for (a) O_2 and (b) N_2. Black lines/circles indicate data between day 2 and day 3 when the wind strengthens. Red lines/circles indicate data between day 3 and day 4.5 when the wind levels off and weakens. N11 is the parameterization suggested by *Nicholson et al.* [2011], N16 [*Nicholson et al.*, 2016] is N11 with revised parameters, and L13 is the formula suggested by *Liang et al.* [2013].

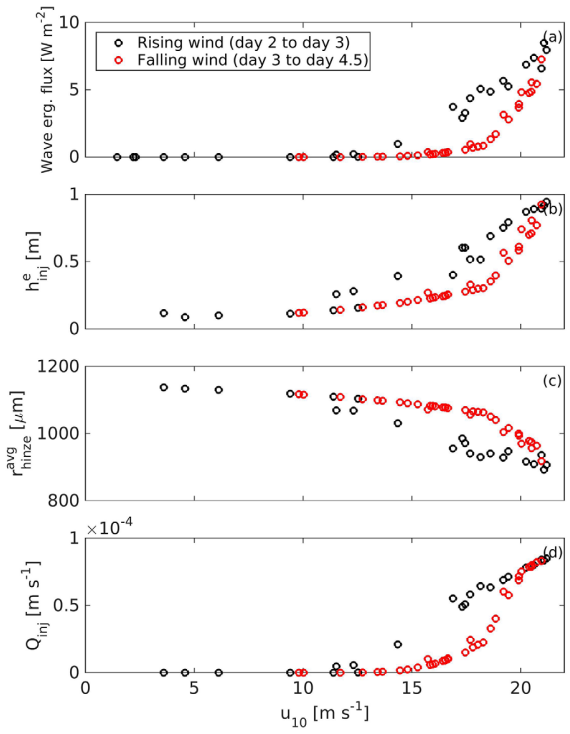

Figure 10. (a) Wave energy flux ($\mathcal{E}$) calculated using Terray's relation [*Terray et al.*, 1996] during rising and falling wind; (b) *e*-folding depth of injected air using the breaking wave model by *Sullivan et al.* [2007] during rising and falling wind; (c) Hinze scale weighted averaged by injected air amount during rising and falling wind; and (d) the rate of injected air during rising and falling wind.

wind speed is increasing most rapidly, between approximately 16 and 19 m s^{-1}, bubble gas flux is more than twice what it is during falling winds although gas saturation anomalies are slightly higher during rising wind (0.81% for O_2 and 0.41% for N_2) than during falling wind (0.14% for O_2 and 0.27% for N_2). The larger gas flux during rising wind than during falling wind is also observed under a hurricane [*D'Asaro and McNeil*, 2015]. When the wind strengthens, its duration is not sufficiently long for the waves to fully develop, and waves are relatively weak with respect to the concurrent wind with a small wave age compared to fully developed waves (mature sea). This condition is favorable for bubble gas flux for the following reasons. (1) More energy is transferred to the ocean and is dissipated for the same wind speed [*Terray et al.*, 1996] (Figure 10a), consequently, more energy is consumed to deposit gas bubbles into the ocean. (2) There are less breaking waves but the waves are steeper and breaking waves are therefore larger in a developing sea [*Sutherland and Melville*, 2015], resulting in bubbles being entrained to a greater depth (Figure 10b). (3) There are relatively more small bubbles in a developing sea, as larger energy dissipation rate in larger breaking waves entails a smaller Hinze scale [*Deane and Stokes*, 2002] (Figure 10c). Physically, stronger turbulence in larger breaking waves is capable of fragmenting smaller bubbles. (4) The rate of air injection is generally larger during rising wind than during falling wind (Figure 10d), though the difference is less evident at wind speed larger than about 20 m s^{-1}. At these wind speeds, the wave energy flux difference between rising and falling wind is not as large as when the wind is weaker because wave was still developing when wind just started weakening. Also, more energy is required to overcome the gravity for deeper air entrainment during rising wind than during falling. All four favorable conditions are captured in the bubble model. A less-developed wave field does entail weaker Langmuir turbulence (Figure 4b) and reduced trapping of bubbles in coherent structures within the turbulent flows [e.g., *Liang et al.*, 2012]. However, the bubble-mediated gas flux is larger for smaller wave ages (Figure 9), implying that gas flux increases from the bubble deposition effect dominates over gas flux decreases due to the Langmuir turbulence effects. The combination of deep breaking-wave bubble deposition and weak Langmuir turbulence also explains the partitioning between fluxes through completely and partially dissolved bubbles. In a developing sea with greater prevalence of large breaking waves, the partially dissolved bubbles, which are large and are usually unable to be subducted by boundary layer turbulence, are entrained to a greater depth by those large breaking waves and play a more important role in gas transfer. Therefore, contribution from partially dissolved bubbles is more significant than that from completely dissolved bubbles while waves are developing (day 2 to day 3), while the contributions from both types of bubbles are similar during fall winds (day 3 to day 4.5) (insets in Figure 7).

Three bubble-mediated gas flux parameterizations, by *Nicholson et al.* [2011, 2016] and by *Liang et al.* [2013], respectively, are also compared with the simulated flux in Figure 9. These three parameterizations are closest to modeled gas fluxes in this study. The difference between fluxes computed using formulas proposed by *Liang et al.* [2013] and those diagnosed in this study is due to the inclusion of wave conditions in this study and correspondingly different bubble parameters, including air deposition amount, bubble deposition depth, and the temporal variability of the Hinze scale. The parameters used in this study are

calibrated with observed gas concentrations and are more reliable than those in *Liang et al*. [2013]. None of them is able to distinguish the difference at different wave conditions. Slight differences between rising wind and falling wind in those parameterization is due to differences in atmospheric pressure.

5. Summary and Conclusion

In this study, a Lagrangian bubble model embedded in a large eddy simulation framework for mechanistic simulation of turbulence, bubbles and gases are presented. In addition to its numerical and computation advantages over Eulerian bubble concentration models, the Lagrangian bubble model allows straightforward separation between completely and partially dissolved bubbles, which is crucial to the accurate quantification of the bubble-mediated gas flux. The model reproduces the evolution of mixed-layer temperature and gas contents from observations under a winter storm at Ocean Station Papa. During the storm period, bubbles play the most important role in the elevation of gas concentration, while most of the variability in gas saturation anomaly is due to the variability in atmospheric pressure. The results also show that waves are an important parameter for bubble-mediated gas flux at transient wind conditions. Contrary to a previous study [*Woolf*, 2005], which concludes that gas transfer rate increases with wave age by assuming both whitecap coverage and bubble generation increase with wave age, this study demonstrates that bubble-mediated gas flux can be stronger when waves are less well developed. For the same wind speed, bubble-mediated gas fluxes during strengthening winds could be twice as much as during weakening winds, even though gas saturation anomaly is higher during the period of strengthening winds. When wind strengthens, waves are less-developed with respect to wind, resulting in more frequent large breaking waves. Bubble generation in large breaking waves is favorable for a large bubble-mediated gas flux. Existing parameterizations for bubble-mediated gas flux do not include any wave forcing. While the limited and variable wind and wave conditions during the short period in this study do not permit a direct derivation of a full wave-dependent parameterization, the calibrated model developed in this study will carry forward to simulations with controlled wave conditions with the goal of deriving a wave-dependent parameterization in future studies.

Acknowledgments

This study is supported by the National Science Foundation through grants, OCE1558317, OCE1558476, OCE1521018, OCE0549887, and OCE0850551, and by the Office of Naval Research through grants N00014-081-0577 and N00014-081-0575, and through postdoc support provided by the Applied Physics Laboratory at the University of Washington. Computations were performed using supercomputing facilities at Louisiana State University and at the National Center for Atmospheric Research. Physical measurements from the NOAA surface mooring are available from http://www.pmel.noaa.gov/OCS/Papa. Gas measurements from the NOAA surface mooring are available at http://www.pmel.noaa.gov/co2/story/Papa. Wave data are available at http://www.apl.washington.edu/projects/station_papa/summary.html. Model solutions and data for figures are available from the corresponding author Jun-Hong Liang (jliang@lsu.edu). This is PMEL publication #4563.

References

Asher, W. E., P. J. Farley, B. J. Higgins, L. M. Karle, E. C. Monahan, and I. S. Leifer (1996), The influence of bubble plumes on air/seawater gas transfer velocities, *J. Geophys. Res.*, *101*, 12,027–12,041.

Baschek, B., D. M. Farmer, and C. Garrett (2006), Tidal fronts and their role in air-sea gas exchange, *J. Mar. Res.*, *64*, 483–515.

Blenkinsopp, C. E., and J. R. Chaplin (2007), Void fraction measurements in breaking waves, *Proc. R. Soc. A*, *463*, 3151–3170.

Bushinsky, S., and S. Emerson (2015), Marine biological production from in situ oxygen measurements on a profiling float in the subarctic Pacific Ocean, *Global Biogeochem. Cycles*, *29*, 2050–2060, doi:10.1002/2015GB005251.

Craik, A. D. D., and S. Leibovich (1976), A rational model for Langmuir circulations, *J. Fluid Mech.*, *73*, 401–426.

Cronin, M. F., N. A. Pelland, S. R. Emerson, and W. R. Crawford (2015), Estimating diffusivity from the mixed layer heat and salt balances in the North Pacific, *J. Geophys. Res. Oceans*, *120*, 7346–7362, doi:10.1002/2015JC011010.

D'Asaro, E. A., and C. McNeil (2007), Air-sea gas exchange at extreme winds speeds measured by autonomous oceanographic floats, *J. Mar. Res.*, *66*, 92–109.

D'Asaro, E. A., and C. McNeil (2015), Wave effects on gas transfer rates under hurricane force winds, Book of abstract, paper presented at 7th International Symposium on Gas Transfer at Water Surface, University of Wash., Washington, D. C. [Available at http://depts.washington.edu/uwconf/wordpress/gtws7/.] [Available at http://depts.washington.edu/uwconf/gtws7/GTWS7_Abstract_Book.pdf.]

Deane, G. B., and M. D. Stokes (2002), Scale dependence of bubble creation mechanisms in breaking waves, *Nature*, *418*, 839–844.

Deike, L., W. K. Melville, and S. Popineta (2016), Air entrainment and bubble statistics in breaking waves, *J. Fluid Mech.*, *801*, 91–129.

Emerson, S., and S. Bushinsky (2016), The role of bubbles during air-sea gas exchange, *J. Geophys. Res. Oceans*, *121*, 4360–4376, doi:10.1002/2016JC011744.

Emerson, S., C. Stump, B. Johnson, and D. Karl (2002), In situ determination of oxygen and nitrogen dynamics in the upper ocean, *Deep Sea Res., Part I*, *49*, 941–952.

Emerson, S., C. Stump, and D. Nicholson (2008), Net biological oxygen production in the ocean: Remote in situ measurements of O_2 and N_2 in surface waters, *Global Biogeochem. Cycles*, *22*, GB3023, doi:10.1029/2007GB003095.

Fairall, C. W., E. F. Bradley, J. E. Hare, A. A. Grachev, and J. B. Edson (2003), Bulk parameterization of air-sea fluxes: Updates and verification for the COARE algorithm, *J. Clim.*, *16*, 571–591.

Fairall, C. W., M. Yang, L. Bariteau, J. B. Edson, D. Helmig, W. McGillis, S. Pezoa, J. E. Hare, B. Huebert, and B. Blomquist (2011), Implementation of the coupled ocean-atmosphere response experiment flux algorithm with CO_2, dimethyl sulfide, and O_3, *J. Geophys. Res.*, *116*, C00F09, doi:10.1029/2010JC006884.

Farmer, D., and M. Li (1995), Patterns of bubble clouds organized by Langmuir circulation, *J. Phys. Oceanogr.*, *25*, 1426–1440.

Farmer, D. M., C. L. McNeil, and B. D. Johnson (1993), Evidence for the importance of bubbles in increasing air-sea gas flux, *Nature*, *361*, 620–623.

Fassbender, A. J., C. L. Sabine, and M. F. Cronin (2016), Net community production and calcification from7 years of NOAA Station Papa Mooring measurements, *Global Biogeochem. Cycles*, *30*, 250–267, doi:10.1002/2015GB005205.

Fuchs, G., W. Roether, and P. Schlosser (1987), Excess ^{3}He in the ocean surface layer, *J. Geophys. Res.*, *92*, 6559–6568.

Garcia, H. E., R. A. Locarnini, T. P. Boyer, J. I. Antonov, O. K. Baranova, M. M. Zweng, J. R. Reagan, and D. R. Johnson (2014), World Ocean Atlas 2013, vol. 3, Dissolved oxygen, apparent oxygen utilization, and oxygen saturation, edited by S. Levitus and A. Mishonov (Technical Ed.), *NOAA Atlas NESDIS 75*, 27 pp. [Available at https://data.nodc.noaa.gov/woa/WOA13/DOC/woa13_vol3.pdf.]

Goddijn-Murphy, L., D. K. Woolf, and C. Marandino (2012), Space-based retrievals of air-sea gas transfer velocities using altimeters: Calibration for dimethyl sulfide, *J. Geophys. Res.*, *117*, C08028, doi:10.1029/2011JC007535.

Goddijn-Murphy, L., D. K. Woolf, A. H. Callaghan, P. D. Nightingale, and J. D. Shutler (2016), A reconciliation of empirical and mechanistic models of the air-sea gas transfer velocity, *J. Geophys. Res. Oceans*, *121*, 818–835, doi:10.1002/2015JC011096.

Hamlington, P. E., L. P. V. Roekel, B. Fox-Kemper, K. Julien, and G. P. Chini (2014), Langmuir-submesoscale interactions: Descriptive analysis of multiscale frontal spin-down simulations, *J. Phys. Oceanogr.*, *44*, 2249–2272.

Hamme, R. C., and S. R. Emerson (2002), Mechanisms controlling the global oceanic distribution of the inert gases argon, nitrogen and neon, *Geophys. Res. Lett.*, *29*(23), 2120, doi:10.1029/2002GL015273.

Harcourt, R. R., and E. A. D'Asaro (2008), Large-eddy simulation of Langmuir turbulence in pure wind seas, *J. Phys. Oceanogr.*, *38*(7), 1542–1562, doi:10.1175/2007JPO3842.1.

Hinze, J. O. (1955), Fundamentals of the hydrodynamic mechanism of splitting in dispersion processes, *AIChE J.*, *1*(3), 289–295.

Ho, D. T., R. Wanninkhof, P. Schlosser, D. S. Ullman, D. Hebert, and K. F. Sullivan (2011), Towards a universal relationship between wind speed and gas exchange: Gas transfer velocities measured with $^3He/SF_6$ during the Southern Ocean Gas Exchange Experiment, *J. Geophys. Res.*, *116*, C00F04, doi:10.1029/2010JC006854.

Jähne, B., and H. Haußecker (1998), Air-water gas exchange, *Annu. Rev. Fluid Mech.*, *30*(1), 443–468.

Keeling, R. (1993), On the role of large bubbles in air-sea gas exchange and supersaturation in the ocean, *J. Mar. Res.*, *51*, 237–271.

Kukulka, T., A. Plueddemann, and P. Sullivan (2013), Inhibited upper ocean restratification in nonequilibrium swell conditions, *Geophys. Res. Lett.*, *40*, 3672–3676, doi:10.1002/grl.50708.

Lamarre, E., and W. K. Melville (1991), Air entrainment and dissipation in breaking waves, *Nature*, *351*, 469–472.

Leibovich, S. (1983), The form and dynamics of Langmuir circulations, *Annu. Rev. Fluid Mech.*, *15*, 391–427.

Leifer, I., and R. K. Patro (2002), The bubble mechanism for methane transport from the shallow sea bed to the surface: A review and sensitivity study, *Cont. Shelf Res.*, *22*, 2409–2428.

Li, M., C. Garrett, and E. Skyllingstad (2005), A regime diagram for classifying turbulent large eddies in the upper ocean, *Deep Sea Res., Part I*, *52*, 259–278, doi:10.1016/j.dsr.2004.09.004.

Liang, J.-H., J. C. McWilliams, P. P. Sullivan, and B. Baschek (2011), Modeling bubbles and dissolved gases in the ocean, *J. Geophys. Res.*, *116*, C03015, doi:10.1029/2010JC006579.

Liang, J.-H., J. C. McWilliams, P. P. Sullivan, and B. Baschek (2012), Large eddy simulation of the bubbly ocean: New insights on subsurface bubble distribution and bubble-mediated gas transfer, *J. Geophys. Res.*, *117*, C04002, doi:10.1029/2011JC007766.

Liang, J.-H., C. Deutsch, J. C. McWilliams, B. Baschek, P. P. Sullivan, and D. Chiba (2013), Parameterizing bubble-mediated air-sea gas exchange and its effect on ocean ventilation, *Global Biogeochem. Cycles*, *27*, 894–905, doi:10.1002/gbc.20080.

Long, M. C., K. Lindsay, S. Peacock, J. Keith Moore, and S. C. Doney (2013), Twentieth-century oceanic carbon uptake and storage in CESM1(BGC), *J. Clim.*, *26*(18), 6775–6800, doi:10.1175/JCLI-D-12-00184.1.

Ma, G., F. Shi, and J. T. Kirby (2011), A polydisperse two-fluid model for surf zone bubble simulation, *J. Geophys. Res.*, *116*, C05010, doi:10.1029/2010JC006667.

Manning, C. C., R. H. R. Stanley, D. P. Nicholson, and M. E. Squibb (2016), Quantifying air-sea gas exchange using noble gases in a coastal upwelling zone, *IOP Conf. Ser. Earth Environ. Sci.*, *35*, 012017, doi:10.1088/1755-1315/35/1/012017.

McNeil, C., and E. D'Asaro (2007), Parameterization of air-sea gas fluxes at extreme wind speeds, *J. Mar. Syst.*, *66*, 110–121.

McWilliams, J. C., P. P. Sullivan, C. H. Moeng (1997), Langmuir turbulence in the ocean, *J. Fluid Mech.*, *334*, 1–30.

Melville, W. K., and P. Matusov (2002), Distribution of breaking waves at the ocean surface, *Nature*, *417*, 58–63.

Melville, W. K., F. Verron, and C. J. White (2002), The velocity field under breaking waves: Coherent structures and turbulence, *J. Fluid Mech.*, *454*, 203–233.

Moeng, C.-H. (1984), A large-eddy-simulation model for the study of planetary boundary layer turbulence, *J. Atmos. Sci.*, *41*, 2052–2062.

Nicholson, D., S. Emerson, N. Caillon, J. Jouzel, and R. C. Hamme (2010), Constraining ventilation during deepwater formation using deep ocean measurements of the dissolved gas ratios $^{40}Ar/^{36}Ar$, N_2/Ar, and Kr/Ar, *J. Geophys. Res.*, *115*, C11015, doi:10.1029/2010JC006152.

Nicholson, D. P., S. R. Emerson, S. Khatiwala, and R. C. Hamme (2011), An inverse approach to estimate bubble-mediated air-sea gas flux from inert gas measurements, in *6th International Symposium on Gas Transfer at Water Surfaces*, pp. 223–237, Kyoto Univ. Press, Kyoto, Japan.

Nicholson, D. P., S. Khatiwala, and P. Heimbach (2016), Noble gas tracers of ventilation during deep-water formation in the Weddell Sea, *IOP Conf. Ser. Earth Environ. Sci.*, *35*(1), 012019, doi:10.1088/1755-1315/35/1/012019.

Rabe, T. J., T. Kukulka, I. Ginnis, T. Hara, B. Reichl, E. D'Asaro, R. Harcourt and P. P. Sullivan (2015), Langmuir turbulence under Hurricane Gustav (2008), *J. Phys. Oceanogr.*, *45*, 657–677.

Stanley, R. H. R., W. J. Jenkins, D. E. Lott III, and S. C. Doney (2009), Noble gas constraints on air-sea gas exchange and bubble fluxes, *J. Geophys. Res.*, *114*, C11020, doi:10.1029/2009JC005396.

Sullivan, P. P., and J. C. McWilliams (2010), Dynamics of winds and currents coupled to surface waves, *Annu. Rev. Fluid Mech.*, *42*, 19–42, doi:10.1146/annurev-fluid-121108-145541.

Sullivan, P. P., J. C. McWilliams, and W. K. Melville (2004), The oceanic boundary layer driven by wave breaking with stochastic variability. Part 1. Direct numerical simulation, *J. Fluid Mech.*, *507*, 143–174.

Sullivan, P. P., J. C. McWilliams, and W. K. Melville (2007), Surface gravity wave effects in the oceanic boundary layer: Large eddy simulation with vortex force and stochastic breakers, *J. Fluid Mech.*, *593*, 405–452, doi:10.1017/S002211200700897X.

Sutherland, P., and W. K. Melville (2013), Field measurements and scaling of ocean surface wave-breaking statistics, *Geophys. Res. Lett.*, *40*, 3074–3079, doi:10.1002/grl.50584.

Sutherland, P., and W. K. Melville (2015), Field measurements of surface and near-surface turbulence in the presence of breaking waves, *J. Phys. Oceanogr.*, *45*, 943–965.

Suzuki, N., and B. Fox-Kemper (2016), Understanding Stokes forces in the wave-averaged equations, *J. Geophys. Res. Oceans*, *121*, 3579–3596, doi:10.1002/2015JC011566.

Takahashi, T., et al. (2002), Global sea-air CO_2 flux based on climatological surface ocean pCO_2, and seasonal biological and temperature effects, *Deep Sea Res., Part II*, *49*(9–10), 1601–1622.

Terray, E. A., M. A. Donelan, Y. C. Agrawal, W. M. Drennan, K. K. Kahma, A. J. Williams III, P. A. Hwang, and S. A. Kitaigorodskii (1996), Estimates of kinetic energy dissipation under breaking waves, *J. Phys. Oceanogr.*, *26*, 792–807.

Thomson, J., E. A. D'Asaro, M. F. Cronin, W. E. Rogers, R. R. Harcourt, and A. Shcherbina (2013), Waves and the equilibrium range at ocean weather station p, *J. Geophys. Res. Oceans*, *118*, 5951–5962, doi:10.1002/2013JC008837.

Thorpe, S. A. (2004), Langmuir circulation, *Annu. Rev. Fluid Mech.*, *36*, 55–79.

Vagle, S., C. McNeil, and N. Steiner (2010), Upper ocean bubble measurements from the NE pacific and estimates of their role in air-sea gas transfer of the weakly soluble gases nitrogen and oxygen, *J. Geophys. Res.*, *115*, C12054, doi:10.1029/2009JC005990.

Van Roekel, L. P., B. Fox-Kemper, P. P. Sullivan, P. E. Hamlington, and S. R. Haney (2012), The form and orientation of Langmuir cells for misaligned winds and waves, *J. Geophys. Res.*, *117*, C05001, doi:10.1029/2011JC007516.

Wanninkhof, R. (1992), Relationship between wind speed and gas exchange over the ocean, *J. Geophys. Res.*, *97*(C5), 7373–7382, doi: 10.1029/92JC00188.

Wanninkhof, R., W. E. Asher, D. T. Ho, C. Sweeney, and W. R. McGillis (2009), Advances in quantifying air-sea gas exchange and environmental forcing, *Annu. Rev. Mar. Sci.*, *1*, 213–244.

Weil, J. C., P. P. Sullivan, and C.-H. Moeng (2004), The use of large-eddy simulations in Lagrangian particle dispersion models, *J. Atmos. Sci.*, *61*, 2877–2887.

Woolf, D. K. (1997), Bubbles and their role in gas exchange, in *The Sea Surface and Global Change*, edited by P. S. Liss and R. A. Duce, pp. 173–205, Cambridge Univ. Press, Cambridge, U. K.

Woolf, D. K. (2005), Parametrization of gas transfer velocities and sea-state-dependent wave breaking, *Tellus, Ser. B*, *57*, 87–94.

Woolf, D. K., and S. A. Thorpe (1991), Bubbles and the air-sea exchange of gases in near-saturation conditions, *J. Mar. Res.*, *49*, 435–466.